Journal Name

ARTICLE

Hierarchical TiO₂/C nanocomposite monoliths with a robust scaffolding architecture, mesopore-macropore network and TiO₂-C heterostructure for high-performance lithium ion batteries

Hai-Bo Huang,[a]† Yue Yang,[b]† Li-Hua Chen,[*b] Yun Wang,[a] Shao-Zhuan Huang,[b] Jia-Wei Tao,[a] Xiao-Ting Ma,[a] Tawfique Hasan,[c] Yu Li,[b] Yan Xu[*a] and Bao-Lian Su[*b,d,e]

Engineering hierarchical structures of electrode materials is a powerful strategy for optimizing the electrochemical performance of an anode material for lithium-ion batteries (LIBs). Herein, we report the fabrication of hierarchical TiO₂/C nanocomposite monoliths by mediated mineralization and carbonization using bacterial cellulose (BC) as a scaffolding template as well as a carbon source. TiO₂/C has a robust scaffolding architecture, a mesopore-macropore network and TiO₂-C heterostructure. TiO₂/C-500, obtained by calcination at 500 °C in nitrogen, contains anatase TiO₂-C heterostructure with a specific surface area of 66.5 $m^2 g^{-1}$. When evaluated as an anode material at 0.5 C, TiO₂/C-500 exhibits high and reversible lithium storage capacity of 188 mA h g^{-1}, excellent initial capacity of 283 mA h g^{-1}, long cycle life with 94 % coulombic efficiency preserved after 200 cycles, and very low charge transfer resistance. The superior electrochemical performance of TiO₂/C-500 is attributed to the synergistic effect of high electrical conductivity, anatase TiO₂-C heterostructure, mesopore-macropore network and robust scaffolding architecture. The current material strategy affords a general approach for the design of complex inorganic nanocomposites with structural stability, and tailorable and interconnected hierarchical porosity that may lead to next generation of electrochemical supercapacitors with high energy efficiency and superior power density.

Introduction

LIBs are the most successful electrochemical power sources for portable electronics and electric vehicles, due to their advantages of high energy density, long lifespan and no memory effect.[1] In recent years, substantial efforts have been made to develop safe, cost-effective and environmental friendly electrode materials for LIBs. In this context, TiO₂ is considered as one of the most promising materials for LIBs due to a number of advantages in addition to easy availability, structural stability and environmental friendliness:[2] (1) TiO₂ has comparably low density and molar mass offering excellent volumetric and gravimetric storage capacity, (2) owing to its higher working voltage than graphite, TiO₂ anodes can avoid problems like irreversible capacity loss during the formation of a solid-electrolyte interface (SEI) layers while offering improved safety compared to carbon-based electrode materials,[3] and (3) TiO₂ anodes may exhibit significantly extended cycle life due to the formation of a Li₂O buffering matrix upon electrochemical reaction.[4] Considerable efforts have been devoted to unveiling the potential of crystalline TiO₂, especially anatase TiO₂, as an electrode material for LIBs.[5] The challenges for transforming TiO₂ electrode materials to practical applications arise from their poor electrical conductivity and low diffusivity of Li⁺ ions in the lattice structure.[6] Li⁺ diffusivity in TiO₂ can be improved by reducing the size of crystalline TiO₂ to nanoscale[7] as manifested by nanostructured crystalline TiO₂ like nanoparticles,[8] nanowires,[9] nanotubes[10] and nanorods[11] due to high surface-to-volume ratio, short diffusion path and shifted electronic band structure.[12] The improved storage and rate capacity of nanostructured TiO₂ materials goes hand-in-hand with low volumetric capacity and low energy density due to relatively low packing density. In addition, the inherent irregular nanopores in nanostructured TiO₂ hinder the diffusion of electrolyte. It can be anticipated that rendering nanostructured TiO₂ materials with interconnected hierarchical porosity at meso/macrometer scale may improve the packing density,[13] and enhance Li⁺ diffusion/migration in electrolyte and transportation/storage in electrode.[14]

Considerable efforts have been made to developing high efficiency and durable electrode materials for LIBs by

a. State Key Lab of Inorganic Synthesis and Preparative Chemistry, Jilin University, Changchun, 130012, China. E-mail: yanxu@jlu.edu.cn
b. State Key Laboratory of Advanced Technology for Materials Synthesis and Processing, Wuhan University of Technology, 430070, Wuhan, China. E-mail: chenlihua@whut.edu.cn; baoliansu@whut.edu.cn
c. Cambridge Graphene Centre, University of Cambridge, Cambridge, CB3 0FA, UK.
d. Laboratory of Inorganic Materials Chemistry, University of Namur, B-5000 Namur, Belgium. E-mail: bao-lian.su@unamur.be
e. Department of Chemistry and Clare Hall, University of Cambridge, Cambridge, CB2 1EW, UK. E-mail: bls26@cam.ac.uk
f. † These authors contributed equally to this work

incorporating interconnected hierarchical porosity. Hu *et al* developed a hierarchically nanostructured TiO_2 with a 3D network at nano/micrometer scale, showing high electrical conductivity and electrochemical performance.[15] Su *et al* developed a 3DOMM TiO_2 (three-dimensionally ordered macroporous TiO_2 with inner-particle mesopores) with a mesopore-macropore network and high specific surface area.[16] The presence of bimodal porosity with inter-pore connectivity renders 3DOMM TiO_2 better electrochemical performance than that of 3DOM TiO_2 (three-dimensionally ordered macroporous TiO_2). Lee *et al* developed a one-pot method for the synthesis of TiO_2 materials with hierarchical porosity.[17] Compared to mesoporous TiO_2, hierarchical porous TiO_2 exhibits greater reversible capacity and better rate capability due to improved transportation property rendered by interconnected hierarchical porosity. Unfortunately, expensive organic additives are usually required for the synthesis of hierarchical porous structures that hinders large-scale applications. In addition, removal of organic additives may alter the surface chemistry and negatively impact their functional performance during applications.[18]

Improving the electrical conductivity can significantly enhance the electrochemical performance of TiO_2 as an anode material for LIBs. A general approach employed is by addition of conductive components, such as carbon species, forming a TiO_2/carbon composite. Common sources for conductive carbon include carbon precursors such as PAN, PVP and PVA,[13b,19] graphene[20] and CNT/MWCNT.[21] The conductive carbon in TiO_2/carbon renders high electrical conductivity by encapsulating crystalline TiO_2 forming a carbon-coated TiO_2.[19a] So far, the reported TiO_2/carbon composites are often challenged by poor carbon-TiO_2 interface that impedes their application as energy storage devices.[20] In addition, complex synthesis route using expensive precursors and hazardous additives such as benzyl alcohol increases preparation cost and poses environmental concern.[21]

It is therefore of great significance to design a simple route for TiO_2/carbon monoliths with integrated advantages of nanoscale effects, desired porous hierarchy, well-grown carbon-TiO_2 heterostructure and high packing density, leading to functional optimization. Such a TiO_2/carbon monolith, to the best of our knowledge, has not yet been explicitly exploited. In this work, we describe the fabrication of hierarchical TiO_2/C nanocomposite monoliths with a scaffolding architecture and interconnected hierarchical porosity. It is realized by mediated mineralization and carbonization using bacterial cellulose (BC) as a bifunctional agent: (i) scaffolding template and (ii) carbon source. We chose BC aerogel due to its hydroxyl-rich surface capable of mediating the mineralization of titania and also for its carbon-rich composition.[22] By confined hydrolysis and condensation of titanium precursor in the presence of BC, amorphous $BC@TiO_2$ monoliths bearing structural features reminiscent of BC are first obtained. Carbonization in nitrogen atmosphere produces hierarchical TiO_2/C nanocomposite monoliths with the mesopore-macropore network and electrical conductivity depending on the carbonization temperature. When evaluated

as an anode material for LIBs at 0.5 C, TiO_2/C-500, prepared by carbonization at 500 °C, exhibits high and reversible lithium storage capacity of 188 mA h g^{-1}, excellent initial capacity of 283 mA h g^{-1}, long cycle life and very low charge transfer resistance. Systematic investigation reveals the structure-enabled functional performance of TiO_2/C as an anode material. The ability to design scaffolding templates with desired structural hierarchy and surface functionalities allow the development of wide-ranging complex inorganic nanomaterials displaying multi-length scale structural hierarchy for advanced applications.

Experimental

Materials. Sodium hydroxide (NaOH, AR), anhydrous acetic acid (HAc, AR), disodium hydrogen phosphate (Na_2HPO_4, AR), monopotassium phosphate (KH_2PO_4, AR) and potassium bromide (KBr, AR) were purchased from Beijing Chemicals Company, China. D-glucose anhydrous was purchased from AMRESCO LLC, yeast extract was from OXOID, UK and lacto-peptone was from Beijing Aoboxing Biotechonology Company. Ethanol (> 99.9 %) and *tert*-butanol, were purchased from Beijing Chemicals Company. Tetraethyl titanate (TEOT, 33-35 % TiO_2) was purchased from Aladdin. Deionized water was used in all experiments. All chemicals were used as received without further purification.

Preparation of BC aerogels. BC hydrogel was produced by the bacterial strain acetobacter xylinum HN001 in a culture medium of 1.0 L DI water containing 25.0 g D-glucose anhydrous, 7.5 g yeast extract, 10.0 g lacto-peptone and 10.0 g monopotassium phosphate. The culturing medium was adjusted to pH ≈ 5.0 using anhydrous acetic acid, and then sterilized at 120 °C for 20 min in autoclave sterilization pot. Culturing was conducted at 30 °C for 7 d under static conditions. The BC hydrogel (round pellicle with approximate dimensions of 7.0 cm in diameter and 0.7 cm in thickness) was purified in 1 M NaOH aqueous solution at 90 °C for 2 h to remove the bacteria and residual reactants from the pellicles, and then washed with deionized water till pH reached 7.0. After solvent exchange (water dispersing medium was exchanged with a lower surface energy solvent such as ethanol and *tert*-butanol) and freeze drying process, BC aerogels with hierarchical structure were obtained.

Preparation of amorphous BC@TiO₂ monoliths. Amorphous $BC@TiO_2$ monoliths were prepared using sol-gel method. A typical preparation was performed as follows: 0.08 g BC aerogel was immersed in 15 mL of TEOT for 2 h to ensure BC aerogel were completely filled with TEOT. It was then washed using absolute ethanol for three times, and added to DI water. The reaction was allowed to proceed for 2 h at room temperature under vigorous stirring. The resultant products were washed repeatedly using deionized water and ethanol. The resulting light yellow monoliths were dried at 90 °C.

Preparation of TiO₂/C-T. $BC@TiO_2$ was heated at a ramping rate of 2 °C min^{-1} to 400 °C, 500 °C, 600 °C, 700 °C and 800 °C for 2 h in nitrogen. The resultant products were designated as TiO_2/C-400, TiO_2/C-500, TiO_2/C-600, TiO_2/C-700 and TiO_2/C-

800, respectively. A reference was prepared by heating BC@TiO$_2$ to 500 °C in air for 2 h at a ramping rate of 2 °C min^{-1}, designated as TiO$_2$-500.
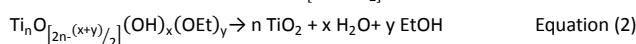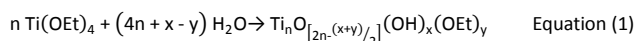
Characterization. Scanning electron microscope (SEM) images were taken on a JEOL JSM 6700F. Transmission electron microscopy (TEM) measurements were conducted on a FEI Tecnai G2S-Twin with a field emission gun operating at 200 kV. Elemental mapping was performed using an EDAX Genesis instrument. Powder X-ray diffraction data (XRD) were acquired on a Rigaku D/Max 2550 with Cu Kα radiation (50 kV, 200 mA), in a 2θ range from 20-80° at a speed of 6° min^{-1}. Energy dispersive spectroscopy (EDS) was conducted on FEI Helios NanoLab 600i. Nitrogen adsorption and desorption isotherms at the temperature of liquid nitrogen were measured on a Micromeritics ASAP 2420 M system. All samples were degassed at 200 °C for 12 h before measurements. Brumauer–Emmett–Teller (BET) method was used to calculate specific surface areas (S$_{BET}$) using adsorption data. The pore size distribution for mesopore was calculated by using the Barrett-Joyner-Halenda (BJH) model, and Density Functional Theory (DFT) model. The pore volumes and pore size distribution were derived from the adsorption branch of isotherms. Macropore size distribution was calculated based on mercury intrusion porosimetry measurements using a Micromeritics AutoPore IV 9500 system. FTIR spectra were collected on a Bruker IFS 66v/S FTIR spectrometer. The thermogravimetry and differential thermal analysis (TG/DTA) were carried out on a NETZSCH STA 449C TG thermal analyzer from 30 °C to 800 °C at a heating rate of 10 °C min^{-1}. X-ray photoelectron spectroscopy (XPS) was performed on an ESCALAB 250 X-ray photoelectron spectrometer using a monochromatic X-ray source.

Electrochemical characterization. The working electrodes for the electrochemical evaluation were prepared in slurry form containing 70 wt% of TiO$_2$/C-T as an active material, 20 wt% of conductive carbon blacks (Super-P) as a conducting agent, 10 wt% of polyvinylidene fluoride (PVDF) as a binder and 1.5 ml of N-methyl-2-pyrrolidone (NMP, 99.9%) as a dispersant. The resulting slurry was coated on a copper foil, pressed to a thin film and dried at 120 °C for 12 h under vacuum. CR2025 coin cells were assembled in an Ar-filled glove box with Celgard polypropylene as a separator, lithium foil as the counter electrode, and 1 M LiPF$_6$ in ethylene carbonate (EC)–diethyl carbonate (DEC) (1:1 v/v) as the electrolyte. Cyclic voltammetry (CV) measurements were carried out using a CHI 660D electrochemical work station at a scanning rate of 0.2 mV s^{-1}. The charge–discharge tests were performed using a LAND battery tester (CT2001A) in a voltage range of 1–3 V (vs. Li/Li$^+$) at different current density. The electrochemical impedance spectroscopy (EIS) analysis was carried out using Autolab PGSTAT 302N in the frequency range of 100 kHz to 0.01 Hz.

Results and discussion

As shown in Scheme. 1a, TiO$_2$/C monoliths are fabricated in two steps: (1) confined deposition of amorphous TiO$_2$ on BC forming amorphous BC@TiO$_2$ monoliths and (2) phase transition forming crystalline and conductive TiO$_2$/C monoliths. Step 1 is achieved by immersing TEOT-filled BC aerogel in water to allow rapid hydrolysis and condensation to take place. Confined deposition of amorphous TiO$_2$ on BC is driven by hydrogen bond formation between the hydroxyl groups of BC and partially hydrolyzed TEOT (Scheme. 1b, Equation 1 and 2). BC@TiO$_2$ has an average diameter of around 180 nm that is significantly thicker than that of BC (Fig. 1a-1c and S1a-S1c†). It confirms the formation of TiO$_2$ layer on BC with an average layer thickness of around 85 nm. TiO$_2$ is amorphous based on the HRTEM and XRD analysis (Fig. 1d and 1e) and its deposition destroys the crystalline order of cellulose as evidenced by the absence of the characteristic diffraction peaks of crystalline cellulose at 14.2°, 16.6° and 22.4° (JCPDS 03-0289) in BC@TiO$_2$ (Fig. 1e and S1d†).

$$n\, Ti(OEt)_4 + (4n + x - y)\, H_2O \rightarrow Ti_nO_{[2n-(x+y)/2]}(OH)_x(OEt)_y \qquad \text{Equation (1)}$$

$$Ti_nO_{[2n-(x+y)/2]}(OH)_x(OEt)_y \rightarrow n\, TiO_2 + x\, H_2O + y\, EtOH \qquad \text{Equation (2)}$$

The TiO$_2$ deposition on BC shifts the absorption band of 3424 cm^{-1} to 3373 cm^{-1} (Fig. 1f). The absorption band at 1647 cm^{-1}, characteristic of the O-C vibration of BC, downshifts slightly, which is likely due to the interfacial interaction between BC and amorphous TiO$_2$.[23] A similar downshift is observed for the in-plane stretching vibration mode of C–H at 2910 cm^{-1}, which is likely attributed to the steric hindrance imposed by the amorphous TiO$_2$. The peak at 1163 cm^{-1}, attributed to the C–O–C stretching of β–glucosidic linkage, is weaker than that of BC, which further confirms the interfacial interactions between BC and TiO$_2$ in BC@TiO$_2$.[24] The TG/DTA data of BC@TiO$_2$ displays a significant weight loss coupled with a sharp exothermic peak between 250 °C and 300 °C, corresponding to the partial decomposition of BC (Fig. S2†). A small weight gain at around 420 °C accompanied with a weak exothermic peak indicates the phase transformation of amorphous TiO$_2$ to anatase TiO$_2$ and the complete decomposition of BC.
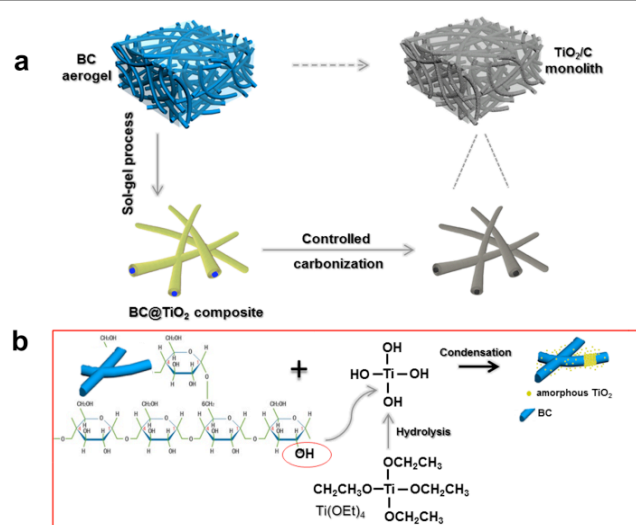
Scheme 1. (a) Schematic illustration of the fabrication process of TiO$_2$/C. (b) Confined deposition of amorphous TiO$_2$ on BC initiated by hydrogen bonding formed between the hydroxyl groups of BC and partially hydrolyzed TEOT.
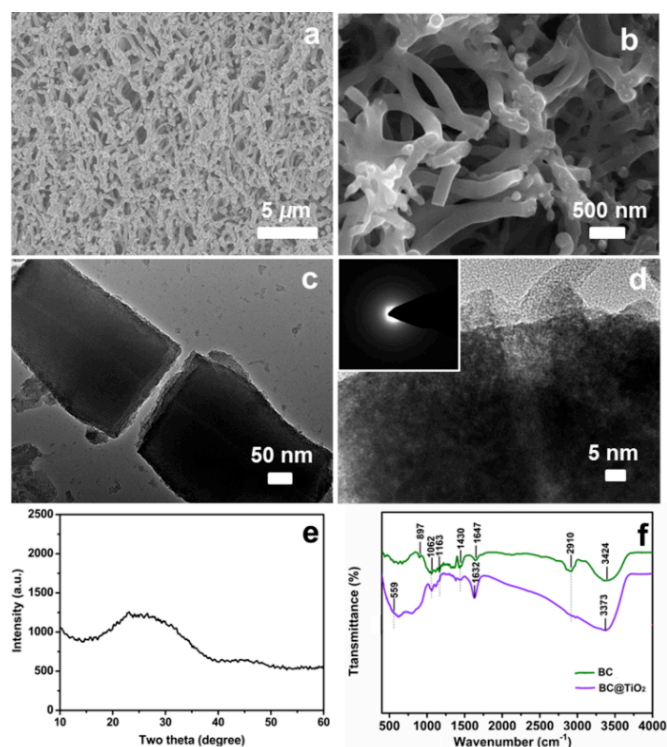
Fig. 1 Characterizing BC@TiO$_2$: (a) Low magnification SEM image showing the scaffolding architecture. (b) SEM image showing the cross-linking of composite fibers with uniform thickness. (c) TEM image showing the presence of BC in fiber core. (d) High magnification TEM showing tiny nanoparticles and inter-particle pores. Inset: SAED pattern showing the amorphous nature of TiO$_2$. (e) XRD pattern. (f) FTIR spectra of BC and BC@TiO$_2$.

Step 2 is realized by calcination of BC@TiO$_2$ in nitrogen giving TiO$_2$/C. For easy recognition, TiO$_2$/C-T (T = calcination temperature) is used in the following context, where the crystalline phase of TiO$_2$ and the degree of carbonization of BC depend on the calcination temperature. Taking TiO$_2$/C-500, for example, it has a hierarchical architecture based on cross-linked composite fibers of TiO$_2$/C-500 with an average diameter of around 200 nm (Fig. 2a). Carbonized BC is clearly visible in the core of the TiO$_2$/C-500 composite fiber with an average diameter of around 25 nm based on the high magnification TEM analysis (Fig. 2b and 2c). TiO$_2$/C-500 contains uniform nanoparticles with an average diameter of around 7.4 nm based on the high magnification TEM. The nanoparticle size of anatase TiO$_2$ is further confirmed using the Scherrer equation ($\tau = K\lambda/\beta cos\vartheta$) (Fig. 2c, Table S1†). Well-crystallized anatase TiO$_2$ phase (JCPDS 21-1272) is identified based on the SEAD and XRD analysis (Fig. 2d Inset, 2e). The average d-spacing of the lattice fringes measured from the HRTEM image is about 0.35 nm, agreeing with the d_{101} plane of anatase TiO$_2$ (Fig. 2d). EDX analysis shows the presence of titanium (Ti), oxygen (O) and carbon (C) (Fig. S3†). It is worth taking note that Ti, O and C distribute uniformly throughout the composite fiber of TiO$_2$/C-500 based on the EDX elemental mapping analysis (Fig. 2f). Notably, calcination in nitrogen atmosphere causes negligible volume change as evidenced by the photographs of BC@TiO$_2$ and TiO$_2$/C-500, which is a very important attribute for applications (Fig. S4†).

The effect of BC on the phase transition of BC@TiO$_2$ during the calcination in nitrogen atmosphere is examined using XRD analysis. As shown in Fig. S5†, anatase TiO$_2$ with relatively low crystallinity is obtained after 2 h at 400 °C. Increasing the calcination temperature increases the crystallinity of anatase TiO$_2$ as evidenced by the XRD patterns of TiO$_2$/C-500 and TiO$_2$/C-600 (Fig. S5†). Calcination at 700 °C in nitrogen causes a partial phase transition of anatase to rutile (JCPDS 87-920), while the anatase/rutile ratio decreases with increasing calcination temperature (Fig. S5†). The results suggest that amorphous TiO$_2$ in BC@TiO$_2$ is transformed to anatase TiO$_2$ at 400 °C, and to rutile TiO$_2$ at temperatures above 700 °C. Peak broadening is observed on the XRD patterns, likely due to the small size of TiO$_2$ crystallites that make up TiO$_2$/C-T. The size of TiO$_2$ nanocrystals of TiO$_2$/C is calculated using the Scherrer equation to be 4.2 nm, 7.0 nm, 12.5 nm, 20.7 nm and 38.8 nm for TiO$_2$/C-400, TiO$_2$/C-500, TiO$_2$/C-600, TiO$_2$/C-700 and TiO$_2$/C-800, respectively (Table S1†). These values are in consistence with the corresponding TEM images (Fig. 2c and S6-S8†). A control sample, TiO$_2$-500, was prepared by calcining BC@TiO$_2$ at 500 °C in air. XRD analysis shows that TiO$_2$-500 contains both anatase and rutile TiO$_2$ phases with sharper and narrower peaks compared to those of TiO$_2$/C-500 (Fig. 2e and S9†). The particle size of TiO$_2$-500 is calculated to be around 9.8 nm using the Scherrer equation, in agreement with the TEM observation (Table S1†, Fig. S10†). It is evident that the carbonization of BC in nitrogen atmosphere contributes to the stabilization of anatase TiO$_2$.
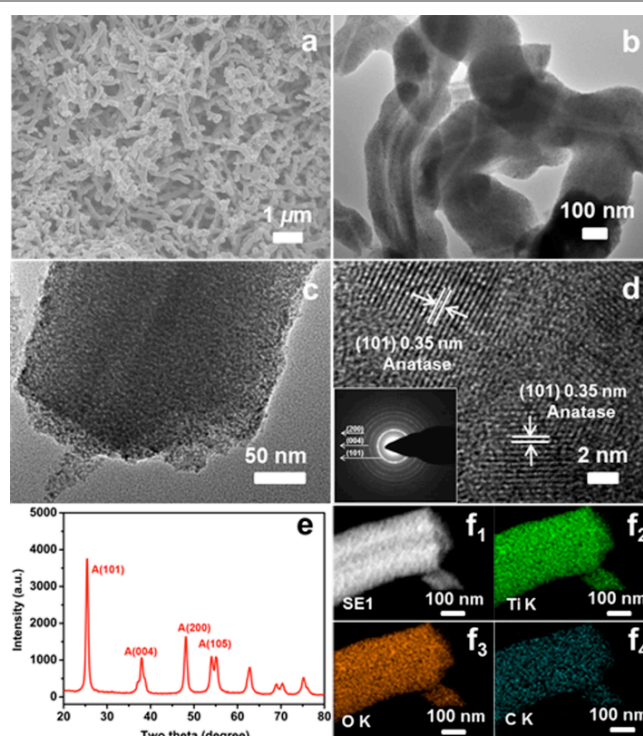

Fig. 2 Characterizing TiO$_2$/C-500: (a) Low magnification SEM image. (b) TEM image showing the presence of carbonized BC at fiber core. (c) High magnification TEM image showing uniform size of nanoparticles and inter-particle pores. (d) HRTEM and SEAD (Inset) showing well crystallized anatase TiO$_2$. (e) XRD. (f$_1$) STEM image and (f$_2$-f$_4$) EDX elemental mapping of Ti, O and C, showing their uniform distribution in the composite fiber.

ARTICLE

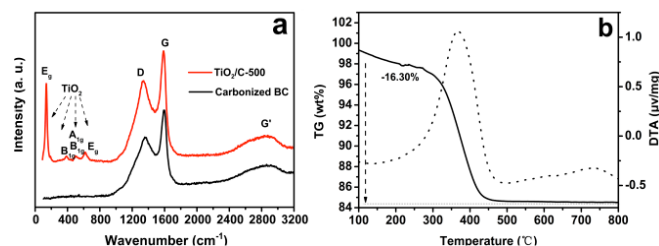**Fig. 3** Characterizing TiO$_2$/C-500: (a) Raman spectra of TiO$_2$/C-500 and carbonized BC aerogel at 500 °C in nitrogen. (b) TG/DTA of TiO$_2$/C-500.

TiO$_2$/C-500 is characterized using Raman spectroscopy (Fig. 3a). Six peaks found on the Raman spectrum at 150 cm^{-1} (E$_g$), 196 cm^{-1} (E$_g$), 398 cm^{-1} (B$_{1g}$), 513 cm^{-1} (A$_{1g}$), 519 cm^{-1} (B$_{1g}$) and 637 cm^{-1} (E$_g$) confirm the presence of anatase TiO$_2$ in TiO$_2$/C-500.[25] The peaks at 1350 cm^{-1} and 1580 cm^{-1}, known as the D-band and the G-band of crystalline graphitized carbon, are attributed to the in-plane vibrations within structured defect and stretching mode of sp^2 carbon, respectively.[26] The sp^2 carbon that is responsible for the increase in overall AC conductivity in this temperature.[27] A control sample was prepared by calcining BC at 500 °C in nitrogen. It is interesting to note that the corresponding carbon peaks of TiO$_2$/C-500 appear to be broader and upshifted compared to those of the carbonized BC at 500 °C, implying the interfacial interaction between anatase TiO$_2$ and carbonized BC. The XPS survey spectrum shows the presence of Ti, O and C in TiO$_2$/C-500 (Fig. S11a†). The deconvoluted XPS signals of Ti 2p (Fig. S11b†) show the typical binding energies of anatase TiO$_2$ at 458.8 eV (Ti 2p$_{3/2}$) and 464.5 eV (Ti 2p$_{1/2}$)[28]. The deconvoluted XPS peak of O1s at 530.7 eV and 532.3 eV are attributed to the lattice oxygen in anatase TiO$_2$ (O$_L$)[29] and bonded oxygen in C–O–Ti,[30] respectively (Fig. S11c†). The deconvoluted XPS peaks of C1s found at 284.7 eV, 258.8 eV and 287.4 eV are attributed to graphitic C=C/C–C, C-O-C, and C=O bond, respectively (Fig. S11d†).[27] The present finding differs from literature report where carbon ions are found in the lattice structure of anatase TiO$_2$.[31] Concurrent TG/DT analysis of TiO$_2$/C-500 reveals a total weight loss of 16.3% in the temperature range of 100-800 °C (Fig. 3b). Two exothermic changes are observed between 200-480 °C and 480-800 °C, respectively. The first thermal change is associated with the decomposition of carbonized BC and the second exothermal change accompanied by a negligible weight loss that is likely attributed to the phase transition of anatase TiO$_2$ to rutile TiO$_2$.

The porous hierarchy of TiO$_2$/C-500 is characterized using nitrogen sorption and mercury porosimetry measurements. It shows a type IV isotherm with narrow mesopores centered at 4 nm and broad mesopores centered at 30 nm calculated using the BJH model from the adsorption branch (Fig. 4a). The BET surface area is calculated to be 66.5 m^2 g^{-1}. Mercury porosity measurements show that TiO$_2$/C-500 contains narrow macorpores centered 0.20 μm (Fig. 4b). The narrow mesopores are derived from inter-particle packing of anatase TiO$_2$. The macropores are formed by cross-linking composite fibers of TiO$_2$/C-500. Notably, BC@TiO$_2$ has a mixed type I-IV isotherm with micropores centered at 1.8 nm calculated using
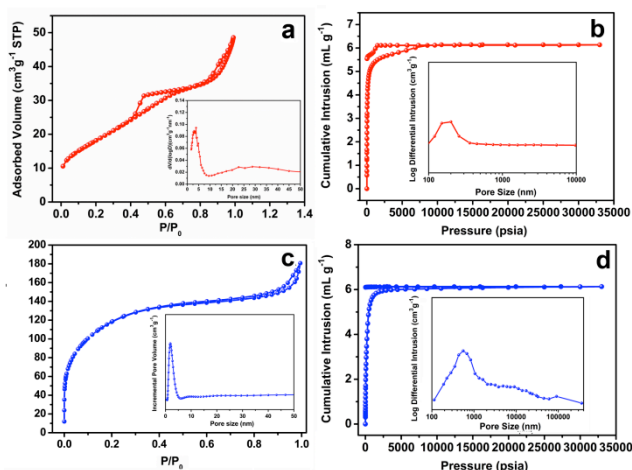

Fig. 4 (a) Nitrogen adsorption-desorption isotherm of TiO$_2$/C-500. Inset showing narrow mesopores centered at 4 nm and broad mesopores centered at 30 nm. (b) Mercury intrusion porosimetry measurement of TiO$_2$/C-500 showing narrow macropores centered at 0.20 μm. (c) Nitrogen adsorption-desorption isotherm of BC@TiO$_2$. Inset showing narrow micropores centered at 1.8 nm. (d) Mercury intrusion porosimetry measurement of BC@TiO$_2$ showing broad and draggy macropores.

the DFT model from the adsorption branch and the BET surface area of 421.6 m^2 g^{-1} (Fig. 4c). The macropores of BC@TiO$_2$ are broad and draggy with an average size significantly larger than those of TiO$_2$/C-500 based on the mercury porosimetry measurements (Fig. 4d). The micropores of BC@TiO$_2$ are textural pores derived from inter-particle packing. The greater inter-particle pores and smaller BET surface area of TiO$_2$/C-500 compared to those of BC@TiO$_2$ are attributed to the larger nanocrystal sizes of anatase TiO$_2$ in TiO$_2$/C-500 than those of the amorphous TiO$_2$ in BC@TiO$_2$ (Fig. 2c, 1d). The broad mesopores centered at 30 nm in TiO$_2$/C-500 are textural pores that are generated by the carbonization of BC. Intriguingly, the macropores of TiO$_2$/C-500 are smaller and narrower compared to those of BC@TiO$_2$, implying that the reassembly of composite fibers occurs during the carbonization of BC@TiO$_2$. We demonstrate that TiO$_2$ nanocrystals can be organized into a scaffolding architecture by simultaneously replicating multi-length scale structural features, namely, mesopores, macropores and monolith (millimeter and above), rendering the TiO$_2$/C-500 monolith multi-length scale structural hierarchy.

TiO$_2$/C-500 monoliths with a robust scaffolding architecture, mesopore-macropore network, high specific surface area and carbon-anatase TiO$_2$ interface may exhibit high electrochemical performance as an anode material for LIBs. The electrochemical behavior of TiO$_2$/C-500 was evaluated in coin type lithium half-cell using Li foil as counter electrode and reference electrode at room temperature. Results show high cycling stability with a charge capacity of 188 mA h g^{-1} after 200 cycles at 0.5 C (Fig. 5a). The excellent cycling performance of TiO$_2$/C-500 is observed likely attributed to the robust scaffolding architecture that is capable of withstanding the repeated insertion/extraction of Li$^+$, and anatase TiO$_2$ nanocrystals facilitate the charge transfer in the electrode/electrolyte interface. TiO$_2$/C-500 outperforms the rest of TiO$_2$/C-T as an anode material for LIBs (Fig. S12†).

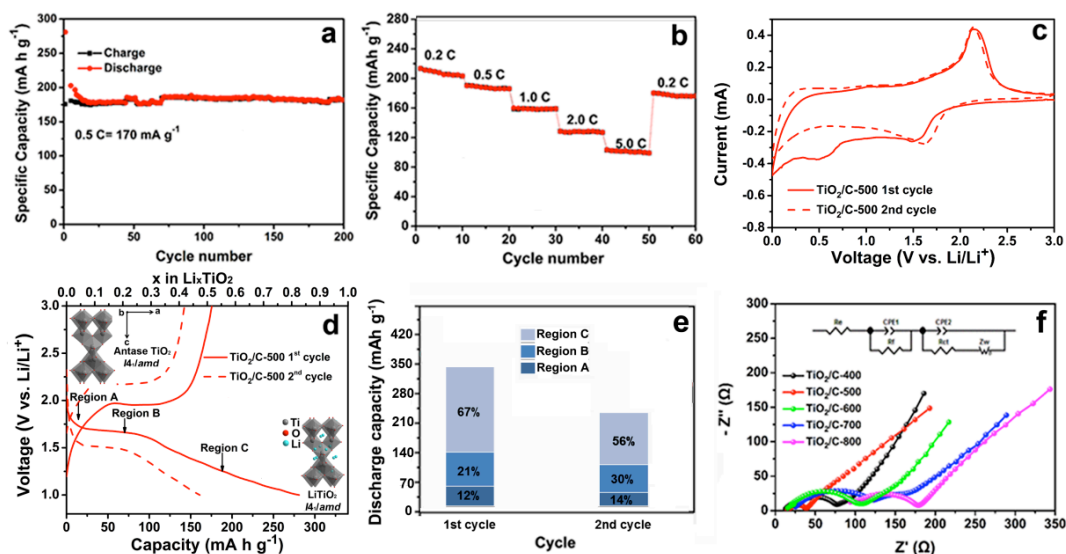**Fig. 5** Electrochemical properties of TiO$_2$/C-500: (a) Cycling performance at 0.5 C. (b) Rate performance. (c) Cyclic voltammograms at a scanning rate of 0.2 mV s^{-1} in the voltage range of 0-3.0 V versus Li/Li$^+$. (d) The first and second charge/discharge profiles at 0.5 C in the voltage range of 0.01-3 V, phase transition upon Li$^+$ insertion in anatase TiO$_2$. (e) Discharge capacity proportions for each characteristic region of the insertion process. (f) Electrochemical impedance spectra of the electrodes after 10 cycles.

Fig. 5b displays the rate capability of TiO$_2$/C-500 at different rates from 0.2 C to 5.0 C. As expected, TiO$_2$/C-500 exhibits high rate capability. When discharged at 0.2 C for 10 cycles, the TiO$_2$/C-500 anode has a discharge capacity of 215 mA h g^{-1} and a subsequent charge capacity of 203 mA h g^{-1}, leading to a high coulombic efficiency of 94%. Increasing the current density to 0.5 C, 1 C and 2 C leads to a decrease in the reversible capacity to 191 mA h g^{-1}, 159 mA h g^{-1} and 128 mA h g^{-1}, respectively. When the current density was 5 C, a capacity of 103 mA h g^{-1} is obtained. The rate performance is noticeable when the capacity values are normalized by their first discharge capacities (Fig. S13†). TiO$_2$/C-500 retains 47.9 % of capacity at 5 C, which is higher than reported anode materials based on hierarchically structured TiO$_2$.[16,32] Reducing the current rate to 0.2 C results in a discharge capacity of 179 mA h g^{-1}. The good rate performance of TiO$_2$/C-500 may be attributed to the well-preserved mesopore-macropore network, which provide easy wettability and facilitate mass transport of electrolytes. We believe that carbon in TiO$_2$/C-500 plays an important role in effectively buffering the structural strain and volume change, and contribute to the fast response at high current rate. In addition, small crystallite sizes and inner-particle mesopores of TiO$_2$/C-500 results in a large quantity of reactive sites, short and continuous path facilitating the diffusion and insertion of Li$^+$, which contribute to the high rate performance of the TiO$_2$/C-500 anode.

The cyclic voltammograms (CV) curves of the TiO$_2$/C-500 anode for the first two cycles at a scan rate of 0.2 mV s^{-1} is shown in Fig. 5c. The redox peak at approximately 1.5-1.7 V corresponds to the characteristic pseudocapacitive behavior of Li$^+$ storage in TiO$_2$/C-500. 1.6-2.2 V is the typical behavior expected of solid-state diffusion of Li$^+$ in anatase TiO$_2$. It is worth taking note that the rectangular shape in the range of 1.0 V-1.7 V is characteristic of charging/discharging of supercapacitance arising from the carbon-anatase TiO$_2$

interface.[21b] The half reaction that governs the electrochemical processes in nanostructured TiO$_2$/Li half-cell is as follows:

$$\text{TiO}_2 + x\,\text{Li}^+ + x\,e^- = \text{Li}_x\text{TiO}_2 \ (x \leq 1) \qquad \text{Equation (3)}$$
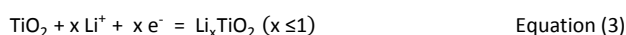
where x is the amount of inserted Li$^+$ in anatase that depends on the crystalline phase and the nanostructural features of TiO$_2$ materials.[33] The function corresponds to the complete reduction of Ti^{4+} to Ti^{3+}, the theoretical capacity of anatase has been reported as 336 mA h g^{-1} (x = 1), while, for the fully reversible reaction, the maximum x is 0.5, corresponding to a capacity of 168 mA h g^{-1}.[34] For x = 0.5, Li$^+$ insertion into anatase TiO$_2$ causes a phase transition from tetragonal TiO$_2$ (space group $I4_1/amd$) to orthorhombic Li$_{0.5}$TiO$_2$ (space group *Imma*). The peaks show little change in voltage position and amplitude during the first two cycles, indicating good stability and high reversibility of the electrochemical reactions occurring in TiO$_2$/C-500.

The charge-discharge profiles of TiO$_2$/C-500 at 0.5 C are shown in Fig. 5d. The voltage profiles of TiO$_2$/C-500 in the first discharge cycle show three distinct regions. The initial open-circuit voltage (OCV) of the cell is ~2.4 V versus Li$^+$/Li. The value of 2.4-3.0 V is typical of an electrode based on carbon and anatase TiO$_2$ versus a Li-metal electrode.[35] Region A (OCV to ~1.75 V) shows a rapid voltage drop associated with the topotactic insertion of Li$^+$ into the anatase TiO$_2$ phase of TiO$_2$/C-500. This process is ascribed to either capacitive-like surface effect[36] or the formation of a solid solution insertion mechanism of TiO$_2$ and Li$_x$TiO$_2$.[33a,35a] The amount of Li$^+$ inserted during this stage depends on the crystallite size and the surface area of active components. The zone between 0 and 33 mA h g^{-1} is associated with homogeneous Li$^+$ insertion into the anatase structure without any phase transition, giving a Li-poor titanate phase of Li$_{0.1}$TiO$_2$. A two-phase plateau in region B (1.76 > V > 1.74 V) corresponds to Li$^+$ insertion into
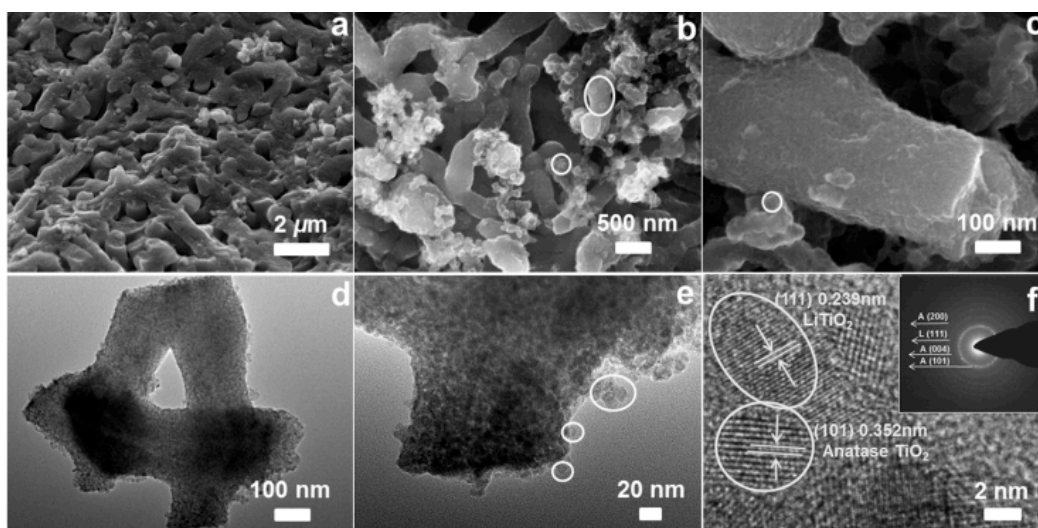
Fig. 6 Characterizing the TiO₂/C-500 anode: (a) Low magnification SEM image. (b) SEM image. (c) High magnification SEM. (d) TEM image. (e) High magnification TEM image. (f) HRTEM image after 150 cycles at 0.5 C. Inset showing the SEAD pattern.

the anatase lattice of TiO₂ followed by Li$^+$ insertion into the surface layer of the electrode. Both Li-rich phase and Li-poor phase are found co-existing in region B.[35b] At 1.75 V versus Li/Li$^+$, the phase transition starts at the beginning and ends at the tail of the voltage plateau, where anatase TiO₂ and Li$_{0.5}$TiO₂, phase (space group *Imma*) coexist. In region C, a gradual voltage decrease is observed after the plateau, indicating topotactic insertion induced by applied potential. The sloped voltage profile is a reflection of structural stability during Li$^+$ insertion-extraction that is attributed to the size effect of TiO₂ nanoparticles and the mesopore-macropore network of TiO₂/C-500 in favor of reversible insertion–extraction and insertion ratios.[35b] The existence of this intercalation domain is related to a second biphasic domain, where more lithium is inserted in the anatase TiO₂ structure as shown by a continuous reduction of Ti^{4+} to Ti^{3+}. The full occupation of octahedral site by Li$^+$ in the structure of LiTiO₂ is present at the end of the discharge.[37] The capacity is in an order of region C > region B > region A derived from the respective discharge curve (Fig. 5e). The results show that TiO₂/C-500 can accommodate 0.85 Li$^+$ per TiO₂ (283 mA h g^{-1}) during the first discharge cycle, which is much higher than the reported values.[17,38] Subsequently, 0.53 mol of Li$^+$ per 1 mol TiO₂ (Li$_{0.53}$TiO₂, 176 mA h g^{-1}) can be cycled reversibly, giving a coulombic efficiency of 63 %. The high initial discharge capacity is attributed to the monolithic nature of TiO₂/C-500 containing a mesopore-macropore network, which enables easy and short transportation of electrolyte for Li$^+$ diffusion. Such a hierarchical porous structure renders high reversibility and good capacity retention during the discharge–charge process (Fig. S14 †). In the second cycle, the profile of charge/discharge curve appears to be the same as the first cycle with the discharge and charge capacity of 162 and 143 mA h g^{-1}, respectively, and a coulombic efficiency of 89 %. The coulombic efficiency of TiO₂/C-500 is 94 % after the third cycle and remains steady after 200 discharge/charge cycles (Fig. S14

†). It implies a rapid Li$^+$ insertion/extraction in the discharge–charge process owing to the mesopore-marcopore network and high surface area of TiO₂/C-500.

Electrochemical impedance spectroscopy (EIS) measurements were performed to provide further information on the electrochemical kinetics of TiO₂/C-500. Fig. 5f shows the Nyquist plots of TiO₂/C-T in the frequency range of 100 kHz to 0.01 Hz after 10 cycles at a current density of 100 mA g^{-1}. In general, an EIS curve displays low, middle and high frequency regions, corresponding to electrolyte resistance, charge transfer resistance and solid-state diffusion of Li$^+$, respectively. The charge transfer resistance, Rct, of TiO₂/C-500 appears to be much lower than the rest of TiO₂/C-T, suggesting easy charge transfer on the electrode/electrolyte interface. We believe that high carbon content, great specific surface area and interconnected hierarchical porosity of TiO₂/C-500 are responsible for the cycling stability and reversible capacity. It is worth mentioning that the monolithic nature of TiO₂/C-500 leads to higher packing density compared to P25 that is a favorable attribute for a high energy density battery system (Fig. S15†).

The structural features of the TiO₂/C-500 anode after 150 discharge-charge cycles are examined using SEM and TEM. The scaffolding architecture based on the cross-linking composite fibers of TiO₂/C-500 is largely preserved after 150 cycles, indicating the good structural stability of TiO₂/C-500 when used as an anode. The aggregates attached to the fiber surface, marked in white circles in Fig. 6b and 6c, are conductive carbon species that serve to improve the electrical conductivity and reduce the polarization of TiO₂/C-500. Cross-linking among the composite fibers is clearly visible, and the composite fibers are comprised of packed nanoparticles with inter-particle pores (Fig. 6d and 6e). Notably, aggregates with sizes below 10 nm are found on the surface of TiO₂/C-500 (white-circled in Fig. 6e). The average *d*-spacing of the lattice fringes measured from the HRTEM image is about 0.239 nm,
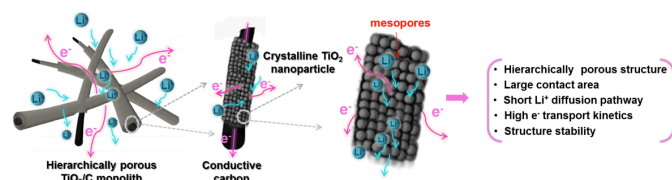
Scheme 2. Illustration of Li$^+$ insertion in the TiO$_2$/C anode.

agreeing with the d_{111} plane of LiTiO$_2$, further confirming the formation of LiTiO$_2$ (JCPDS 16-0223).[33b] Both anatase TiO$_2$ and LiTiO$_2$ are found in TiO$_2$/C-500 after 150 cycles based on the SEAD pattern (Fig. 6f Inset). The results suggest that continuous Li$^+$ insertion into TiO$_2$ causes atomic rearrangement, giving rise to a cubic LiTiO$_2$. The formation of cubic LiTiO$_2$ phase is indicated by the peaks at 43.8° and 63.6°, characteristic of the cubic LiTiO$_2$ phase coupled with weaker XRD peaks of anatase TiO$_2$ (Fig. S16†).[39] We therefore modify the Equation 3 by including the contribution of Li$_x$TiO$_2$ as follows:

$$(1-x)Li^+ + (1-x)\,e^- + Li_xTiO_2 \leftrightarrow LiTiO_2 \qquad \text{Equation (4)}$$
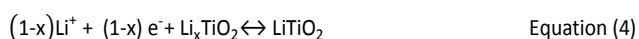
The formation of LiTiO$_2$ enhances the Li$^+$ insertion capability of the TiO$_2$/C-500 anode during the electrochemical process, making TiO$_2$/C-500 a self-diagnostic anode material for LIBs.

The Li$^+$ storage capability of TiO$_2$/C-500 is illustrated in Scheme 2. The hierarchical porous structure of TiO$_2$/C-500 allows easy access of electrolyte, promoting electrolyte-electrode contact. The interconnected mesopore-macropore network facilitates Li$^+$ transportation, reduces pulverization, and improves cycling performance and rate capability. The small nanocrystal size shortens transportation path while the high specific surface area avails more reactivate sites, leading to high coulombic efficiency. The presence of carbon in TiO$_2$/C-500 enhances its electrical conductivity and serves to buffer the structural strain and volume changes during repeated electrochemical reactions.

BC plays multiple roles in the construction of TiO$_2$/C: (1) A general, effective and environmentally friendly bottom-up approach for composite monoliths with scaffolding architecture and tunable porous hierarchy. (2) A carbon source rendering TiO$_2$/C good electrical conductivity by controlled pyrolysis. (3) Increase the phase transition temperature of anatase TiO$_2$ to rutile TiO$_2$ and hinder crystal growth leading to high specific surface area.

Conclusions

A hierarchical BC/TiO$_2$ monolith with scaffolding architecture, a mesopore-macropore network and high specific surface area has been obtained by confined mineralization using BC as a scaffolding template and carbon source. Calcination of BC/TiO$_2$ in nitrogen atmosphere produces TiO$_2$/C monoliths with a scaffolding architecture and mesopore-macropore network reminiscent that of BC while the electrical conductivity and porous hierarchy depending on the calcination temperature.

The presence of BC in BC/TiO$_2$ confines the growth of anatase nanocrystals. The synergistic effect of small nanocrystals, high specific surface area, anatase TiO$_2$ phase, carbon-antase interface, interconnected mesopore-macropore network and robust scaffolding architecture of TiO$_2$/C-500 account for the high lithium storage capacity, excellent initial capacity, superior cycling stability and very low charge transfer resistance. TiO$_2$/C monoliths can be made in a variety of shapes and dimensions that make it a promising choice as high packing density and high-energy efficiency anode material for LIBs. The bioinspired materials strategy may prove its versatility for developing complex inorganic nanomaterials with multi-length scale structural hierarchy and multi-functionality.

Notes and references

1   (*a*) J. B. Goodenough and Y. Kim, *Chem. Mater.*, 2010, **22**, 587-603; (*b*) V. Etacheri, R. Marom, R. Elazari, G. Salitra and D. Aurbach, *Energy Environ. Sci.*, 2011, **4**, 3243-3262.
2   (*a*) M. V. Reddy, G. V. Subba Rao and B. V. R. Chowdari, *Chem. Rev.*, 2013, **113**, 5364-5457; (*b*) T. Xia, W. Zhang, J. B. Murowchick, G. Liu and X. Chen, *Adv. Energy Mater.*, 2013, **3**, 1516-1523.
3   X. Yan, Y. Zhang, K. Zhu, Y. Gao, D. Zhang, G. Chen, C. Wang and Y. Wei, *J. Power Sources*, 2014, **246**, 95-102.
4   Z. Wang, L. Zhou and X. W. Lou, *Adv. Mater.*, 2012, **24**, 1903-1911.
5   (*a*) L. Kavan, M. Grätzel, S. E. Gilbert, C. Klemenz and H. J. Scheel, *J. Am. Chem. Soc.*, 1996, **118**, 6716-6723; (*b*) I. Exnar, L. Kavan, S. Y. Huang and M. Grätzel, *J. Power Sources*, 1997, **68**, 720-722.
6   J. Qiu, P. Zhang, M. Ling, S. Li, P. Liu, H. Zhao and S. Zhang, *ACS Appl. Mater. Interfaces*, 2012, **4**, 3636-3642.
7   Y. S. Hu, L. Kienle, Y. G. Guo and J. Maier, *Adv. Mater.*, 2006, **18**, 1421-1426.
8   Y. Ren, Z. Liu, F. Pourpoint, A. R. Armstrong, C. P. Grey and P. G. Bruce, *Angew. Chem. Int. Ed.*, 2012, **124**, 2206-2209.
9   L. Mai, X. Tian, X. Xu, L. Chang and L. Xu, *Chem. Rev.*, 2014, **114**, 11828-11862.
10 J. Brumbarov, J. P. Vivek, S. Leonardi, C. Valero-Vidal, E. Portenkirchner and J. Kunze-Liebhauser, *J. Mater. Chem. A*, 2015, **3**, 16469-16477.
11 L. C. Kao, C. J. Lin, C. L. Dong, C. L. Chen and S. Y. H. Liou, *Chem. Commun.*, 2015, **51**, 6361-6364.

12 Q. Zhang, E. Uchaker, S. L. Candelaria and G. Cao, *Chem. Soc. Rev.*, 2013, **42**, 3127-3171.

13 (*a*) K. Saravanan, K. Ananthanarayanan and P. Balaya, *Energy Environ. Sci.*, 2010, **3**, 939-948; (*b*) Y. Ma, G. Ji, B. Ding and J. Y. Lee, *J. Mater. Chem*., 2012, **22**, 24380-24385.

14 M. Park, X. Zhang, M. Chung, G. B. Less and A. M. Sastry, *J. Power Sources*, 2010, **195**, 7904-7929.

15 Y. G. Guo, Y. S. Hu, W. Sigle and J. Maier, *Adv. Mater*., 2007, **19**, 2087-2091.

16 J. Jin, S. Z. Huang, J. Liu, Y. Li, D.-S. Chen, H.-E. Wang, Y. Yu, L. H. Chen and B. L. Su, *J. Mater. Chem. A*, 2014, **2**, 9699-9708.

17 J. Hwang, C. Jo, K. Hur, J. Lim, S. Kim and J. Lee, *J. Am. Chem. Soc*., 2014, **136**, 16066-16072.

18 S. K. Das, S. Darmakolla and A. J. Bhattacharyya, *J. Mater. Chem*., 2010, **20**, 1600-1606.

19 (*a*) Z. Yang, G. Du, Q. Meng, Z. Guo, X. Yu, Z. Chen, T. Guo and R. Zeng, *J. Mater. Chem*., 2012, **22**, 5848-5854; (*b*) M. H. Ryu, K. N. Jung, K. H. Shin, K. S. Han and S. Yoon, *J. Phys. Chem. C*, 2013, **117**, 8092-8098.

20 X. Xin, X. Zhou, J. Wu, X. Yao and Z. Liu, *ACS Nano*, 2012, **6**, 11035-11043.

21 (*a*) B. Wang, H. Xin, X. Li, J. Cheng, G. Yang and F. Nie, *Sci. Rep.*, 2014, **4**, 3729; (*b*) N. T. H. Trang, Z. Ali and D. J. Kang, *ACS Appl. Mater. Interfaces*, 2015, **7**, 3676-3683.

22 S. Dutta, A. Bhaumik and K. C. W. Wu, *Energy Environ. Sci*., 2014, **7**, 3574-3592.

23 D. Sun, J. Yang and X. Wang, *Nanoscale*, 2010, **2**, 287-292.

24 C. Wang, E. Yan, Z. Huang, Q. Zhao and Y. Xin, *Macromol. Rapid Commun*., 2007, **28**, 205-209.

25 H. C. Choi, Y. M. Jung and S. B. Kim, *Vib. Spectrosc*., 2005, **37**, 33-38.

26 T. Jawhari, A. Roid and J. Casado, *Carbon*, 1995, **33**, 1561-1565.

27 Y. R. Rhim, D. Zhang, D. H. Fairbrother, K. A. Wepasnick, K. J. Livi, R. J. Bodnar and D. C. Nagle, *Carbon*, 2010, **48**, 1012-1024.

28 Y. Leprince-Wang, *Surf. Coat. Tech*., 2002, **150**, 257-262.

29 S. Sakthivel and H. Kisch, *Angew. Chem. Int. Ed*., 2003, **42**, 4908-4911.

30 T. Xu, W. Hou, X. Shen, H. Wu, X. Li, J. Wang and Z. Jiang, *J. Power Sources*, 2011, **196**, 4934-4942.

31 J. Pouilleau, D. Devilliers, F. Garrido, S. Durand-Vidal and E. Mahé, *Mater. Sci. Eng., B*, 1997, **47**, 235-243.

32 J. Jin, S. Z. Huang, J. Liu, Y. Li, L. H. Chen, Y. Yu, H. E. Wang, C. P. Grey and B. L. Su, *Adv. Sci*., DOI: 10.1002/advs.201500070.

33 (*a*) J. Y. Shin, D. Samuelis and J. Maier, *Adv. Funct. Mater*., 2011, **21**, 3464-3472; (*b*) M. Wagemaker, W. J. H. Borghols and F. M. Mulder, *J. Am. Chem. Soc*., 2007, **129**, 4323-4327.

34 H. Lindström, S. Södergren, A. Solbrand, H. Rensmo, J. Hjelm, A. Hagfeldt and S.-E. Lindquist, *J. Phys. Chem. B*, 1997, **101**, 7710-7716.

35 (*a*) U. Lafont, D. Carta, G. Mountjoy, A. V. Chadwick and E. M. Kelder, *J. Phys. Chem. C*, 2010, **114**, 1372-1378; (*b*) Y. G. Guo, Y. S. Hu and J. Maier, *Chem. Commun*., 2006, 2783-2785.

36 J. Gao, J. Ying, C. Jiang and C. Wan, *J. Power Sources*, 2007, **166**, 255-259.

37 J. Zeng, S. Liu, J. Cai and L. Zhang, *J. Phys. Chem. C*, 2010, **114**, 7806-7811.

38 J. Jin, S. Z. Huang, Y. Li, H. Tian, H. E. Wang, Y. Yu, L. H. Chen, T. Hasan and B. L. Su, *Nanoscale*, 2015, **7**, 12979-12989.

39 K. Jiang, H. Sun and G. Z. Chen, *Chem. Mater*., 2004, **16**, 4324-4329.